

Polarization-based branch selection of bound states in the continuum in dielectric waveguide modes anti-crossed by a metal grating

R KIKKAWA, M NISHIDA and Y KADOYA

Graduate School of Advanced Sciences of Matter, Hiroshima University,
Higashihiroshima 7398530, Japan

E-mail: R. K. (rkikkawa93@gmail.com) or M. N.
(mnishida@hiroshima-u.ac.jp)

Abstract. We investigate bound states in the continuum (BICs) in a planar dielectric waveguide structure consisting of a gold grating on a dielectric layer with a back layer of metal. In this structure, Friedrich-Wintgen (FW) BICs caused by the destructive interference between the radiations from two waveguide modes appear near the anti-crossing point of the dispersion curves. In this study, it is revealed that the branch at which the BIC appears changes according to the polarization of incident radiation. Based on a temporal coupled mode theory, it is shown that the BIC branch is determined by the sign of the product of the coupling coefficients between the two waveguide modes and external radiation, which is consistent with FW theory. The signs of the coupling coefficients are estimated by the waveguide-mode decomposition of the numerically obtained electric fields and are confirmed to vary depending on the polarization.

Keywords: bound states in the continuum, dielectric waveguide, grating

1. Introduction

A bound state in the continuum (BIC) [1,2] is a non-radiative state that lies in the continuous spectral range spanned by the radiation modes. Unlike the quasi-bound states, the BIC, in principle, has an infinitely high quality factor. Although the BIC itself cannot be excited by the incident wave, the Q factor becomes very high near the BIC, which is expected in high-Q devices. The BIC was originally mentioned in Quantum Mechanics in 1929 by Von-Neumann and Wigner [3]. The phenomenon is commonly seen in open-wave systems such as acoustics [4-6], water waves [7,8], and optics [1,9,10]. In optics, the BIC is attracting interest in the context of metasurfaces [11-13], photonic structures [14-18] and plasmonics [19]. It has been shown that quite high Q-values are indeed realized near the BIC [9,20-22], and various nano-photonic/plasmonic applications using BICs have been proposed, such as lasers [23,24], modulators [25], and filters [26], SHG or nonlinear optics [27,28] etc.

Most of the BICs found so far are categorized into two types: the symmetry-protected BIC [9,20,29,30] and the Friedrich-Wintgen (FW) BIC [10,14,15,17,31,32]. The former BIC results from the incompatible symmetry of one of the localized modes with the external radiation field that usually appears at the center of the Brillouin zone (at Γ point). The latter results from the destructive interference of radiations from the two modes that can appear at the off- Γ point around the crossing or anti-crossing point of the dispersion curves of the two modes, depending on the strength of the coupling between them.

We focus on the FW-BIC [32] formed between the two localized modes that are strongly coupled by the near-field overlap with the structural perturbation that produces the coupling to external radiation. In this case, a mode anti-crossing occurs, and the BIC appears on one of the two split-branches. Such a type of BIC is reported in cylindrical resonator system [33-35] and the periodic structures such as photonic [36-39] or plasmonic structures [40]. As is pointed out by Friedrich and Wintgen [32], the regime where the Q factor is kept high around the BIC becomes larger as the near-field coupling becomes stronger. This regime is called the near BIC [40] or the supercavity regime [35] and is targeted in searching for extraordinarily high-Q modes. Therefore, a thorough understanding of the physics behind this type of BIC is quite important for the realization of practical high-Q devices.

The position at which the FW-BIC appears is extremely sensitive to, and dependent on, the structure and parameters of the system. In FW theory [32], it was shown that the shift of the BIC position from the anti-crossing point is determined by the strength of the couplings among the two closed and one open channel based on the Feshbach projection operator method [41]. Moreover, which of the two interfering resonances becomes a BIC was shown to depend on the sign of the product of the matrix elements coupling these channels. Indeed, BICs have been observed on different branches depending on the

system, e.g., on the lower energy branch in a metal relief grating coupled to a dielectric slab waveguide [40], and on the higher energy branch in a low-contrast dielectric grating [36]. Therefore, it is important to understand how the BIC position changes depending on the structure and parameters of the system, in order to characterize the interfering resonances and to determine the optimum design for a high-Q device.

In this study, we demonstrate a phenomenon where the BIC-branch selection is inverted by the polarization of incident light in a dielectric-waveguide/metal-grating structure. If the conclusion of FW theory is applicable to this system, this phenomenon is caused by the sign change of the coupling coefficients among waveguide modes and external radiation. We carry out two actions to confirm this hypothesis. Initially, following temporal coupled mode theory (TCMT) [42,43], which describes general classical open-wave systems, we obtain the BIC condition for the system with two resonant modes and one radiative mode. We pay attention to the signs of the coupling coefficients, and check whether the system conforms to FW theory. Next, we estimate the signs of the coupling coefficients by the waveguide-mode decomposition of the electric fields inside the dielectric layer, which is obtained numerically via the use of a spatial coupled mode theory (SCMT) [44-46], and observe how the sign of the product of the coupling coefficients depends on the polarization of incident light. We note here that SCMT and TCMT are essentially different theories despite their similar names. SCMT is an electromagnetic theory for those systems with a metallic aperture array, wherein Maxwell equations are solved by a modal expansion of electromagnetic fields. On the other hand, TCMT is a more general theory. This method derives a set of equations of motion for simple oscillators whose energy can be transferred to the outside. Therefore, no specific electromagnetic formulation is employed in it.

2. Device structure

We consider a planar dielectric waveguide structure as shown in Fig. 1. It consists of a gold grating on a dielectric layer with a backing metal layer of infinite thickness. Therefore, any wave incident from the grating side is totally reflected except for some absorption. The reflectance as well as the fields inside the device were calculated by the SCMT, for the incident plane wave with S or P polarization, of which the electric or magnetic field has only y-component. The grating with a period of $\Lambda = 433$ nm is composed of a gold strip whose width w_m is 0.98Λ for the P-wave and 0.8Λ for the S-wave. These widths were chosen to facilitate clear observation of the BICs. Note that the grating is 0th order in the air for the wavelength range considered here. To obtain the permittivity of gold, a Drude-Lorentz model fitted to the Johnson-Christy data [47] was used.

3. Calculation Results

We display the dispersion of the 0th order reflectance on the gray scale map for the two polarizations in Fig. 2. In both diagrams, dark bands (low reflectance = high absorption) are clearly seen. The dashed lines indicate the dispersion of the empty lattice modes of the dielectric waveguide sandwiched by the two flat metal planes. We name the lowest order waveguide modes TM_0 and TE_0 , and the second modes, TM_1 and TE_1 for the P- and S-polarizations, respectively. The TE_1 mode is cut off for $\lambda > 1.25 \mu\text{m}$. The dark bands correspond well to the empty lattice modes. Therefore, they are attributed to absorption caused by the metallic loss associated with the dielectric waveguide modes.

At the intersection of the two modes, in both polarizations, one can see an anti-crossing that is caused by the near-field coupling between the two modes induced by the grating. Moreover, near the anti-crossing, the dark band disappeared locally at the positions indicated by the arrows in both polarizations. The disappearance of the absorption corresponds to the BIC. Here a remarkable feature is that the BIC lies on the lower-frequency branch for the P-polarization, whereas it lies on the higher-frequency branch for the S-polarization. This feature is the subject of this study and will be discussed in detail in the next section. However, we first confirm that the disappearance of the absorption is indeed due to the formation of the BIC by evaluating the imaginary part of the eigenfrequency along the upper and lower dark bands for the P-wave and S-wave cases, respectively. In the calculation, the imaginary part of the metal permittivity was removed so that the imaginary part of the eigenfrequency corresponds to the external (radiation) loss. The results are shown in Fig. 3. In both polarizations, the imaginary parts drop to zero at the point where the absorption disappears ($k_x \sim 0.2 [\pi/\Lambda]$), demonstrating that the BICs are indeed formed at that location.

4. Discussion

4.1. Theoretical analysis using TCMT

TCMT describes the behavior of resonances in a system in the time domain. In the present case, the system involves two resonant modes with a near field coupling and a far (radiation) field coupling, the latter via the 0th order grating corresponding to an input/output port. The time evolution of the two mode amplitude $\mathbf{a}^T = (a_1, a_2)$ can be described by an effective Hamiltonian $\tilde{\mathbf{H}}$ and input wave s_+ with a coupling coefficient vector $\mathbf{D} = (d_1, d_2)$ as

$$\frac{d}{dt}\mathbf{a} = -i\tilde{\mathbf{H}}\mathbf{a} + \mathbf{D}^T s_+ = -i\{\boldsymbol{\Omega} - i(\boldsymbol{\Gamma}_i + \boldsymbol{\Gamma}_e)\}\mathbf{a} + \mathbf{D}^T s_+, \quad (1)$$

where

$$\boldsymbol{\Omega} = \begin{pmatrix} \omega_1 & \alpha \\ \alpha & \omega_2 \end{pmatrix}, \boldsymbol{\Gamma}_e = \begin{pmatrix} \gamma_{e1} & \gamma_0 \\ \gamma_0^* & \gamma_{e2} \end{pmatrix}, \boldsymbol{\Gamma}_i = \begin{pmatrix} \gamma_{i1} & 0 \\ 0 & \gamma_{i2} \end{pmatrix}$$

with $\omega_{1,2}$, $\gamma_{i1,2}$ and $\gamma_{e1,2}$ denoting the eigenfrequency, the internal loss, and the external loss of mode 1 or 2, respectively, and $d_{1,2}$ denoting the coupling between the external radiation and modes 1 and 2 through the port. The off-diagonal terms α in $\mathbf{\Omega}$ and γ_0 in $\mathbf{\Gamma}_e$ represent the near- and far-field coupling, respectively. Here, α is set to be real assuming that the effect of material loss on α is negligible, and that the system without material loss has time-reversal symmetry [48]. Considering the principle of the conservation of energy, the outgoing wave s_- can be written as

$$s_- = c_a s_+ + \mathbf{D} \mathbf{a} \quad (2)$$

with c_a representing the direct scattering coefficient.

From time-reversal symmetry and the energy conservation principle, the following relations are derived:

$$\mathbf{D}^\dagger \mathbf{D} = 2\mathbf{\Gamma}_e, \quad (3)$$

$$c_a \mathbf{D}^* = -\mathbf{D}. \quad (4)$$

Using these relations, \mathbf{D} is rewritten as

$$\mathbf{D} = (|d_1|e^{i\varphi_1}, |d_2|e^{i\varphi_2}) = e^{i\varphi_d} (\sqrt{2\gamma_{e1}}, p\sqrt{2\gamma_{e1}}) \quad (5)$$

where φ_d is an arbitrary phase and p is a parity (± 1) that represents the phase difference between d_1 and d_2 . Here $p = 1$ for the in-phase ($|\varphi_1 - \varphi_2| = 0$) case, and $p = -1$ for the anti-phase ($|\varphi_1 - \varphi_2| = \pi$) case. Hereafter, the phase φ_d is set to zero. This is always possible by adjusting the reference position for the external radiation. In addition, the off-diagonal term of $\mathbf{\Gamma}_e$ is rewritten as [42]

$$\gamma_0 = p\sqrt{\gamma_{e1}\gamma_{e2}}. \quad (6)$$

The reflection coefficients for the incident wave with angular-frequency ω can be derived in TCMT from Eqs. (1) and (2) as

$$r(\omega) = c_a \left[1 + 2 \frac{\gamma_{e1}\{i(\omega_2 - \omega) + \gamma_{i2}\} + \gamma_{e2}\{i(\omega_1 - \omega) + \gamma_{i1}\} - i2p\alpha\sqrt{\gamma_{e1}\gamma_{e2}}}{\{(\omega_1 - \omega) - i(\gamma_{i1} + \gamma_{e1})\}\{(\omega_2 - \omega) - i(\gamma_{i2} + \gamma_{e2})\} + (i\alpha + p\sqrt{\gamma_{e1}\gamma_{e2}})^2} \right], \quad (7)$$

as described in the Appendix. The reflectance spectra calculated using Eq. (7) are shown in Figs. 4(c) and 4(d) for $p = 1$ and -1 , respectively, and $\alpha > 0$ for both cases. The parameters used in the calculations, listed in the caption, were decided so as to fit the SCMT results redrawn in Figs. 4(a) and 4(b) from Figs. 2(a) and 2(b) with some magnification. As is clearly seen, the reflectance spectra were accurately reproduced by the TCMT calculation. Importantly, the positions of the BIC are correctly predicted.

The appearance of the BIC is analyzed as follows [36,39,48]. Omitting the internal loss $\mathbf{\Gamma}_i$, the eigenvalues for $\tilde{\mathbf{H}}$ are determined by

$$\left| \tilde{\mathbf{H}} - \omega \mathbf{I} \right| = \{(\omega_1 - \omega) - i\gamma_{e1}\}\{(\omega_2 - \omega) - i\gamma_{e2}\} + (i\alpha + p\sqrt{\gamma_{e1}\gamma_{e2}})^2 = 0, \quad (8)$$

where \mathbf{I} is the identity matrix. If we express the two solutions of Eq. (8) as β and χ , the sum and the product of them yield

$$\beta + \chi = \omega_1 + \omega_2 - i\gamma_{e1} - i\gamma_{e2}, \quad (9)$$

$$\beta\chi = (\omega_1 - i\gamma_{e1})(\omega_2 - i\gamma_{e2}) + (i\alpha + p\sqrt{\gamma_{e1}\gamma_{e2}})^2. \quad (10)$$

When a BIC is realized, one of the solutions is purely real. In that case, the solutions can be expressed using real numbers A and B as

$$\beta = A - i\gamma_{e1} - i\gamma_{e2}, \quad (11)$$

$$\chi = B. \quad (12)$$

By substituting Eqs. (11) and (12) to Eq. (10), the following relations are obtained for A and B ,

$$A + B = \omega_1 + \omega_2, \quad (13)$$

$$AB = \omega_1\omega_2 - \alpha^2. \quad (14)$$

Therefore, A and B are the solutions of the equation

$$x^2 - (\omega_1 + \omega_2)x + \omega_1\omega_2 - \alpha^2 = 0. \quad (15)$$

In addition, by comparing the imaginary parts of both sides of Eq. (10), the expression for B is obtained as

$$B = \frac{\omega_1\gamma_{e2} + \omega_2\gamma_{e1} - 2p\alpha\sqrt{\gamma_{e1}\gamma_{e2}}}{\gamma_{e1} + \gamma_{e2}}. \quad (16)$$

The solutions of Eq. (15) are

$$x_{\pm} = \frac{1}{2}\{\omega_1 + \omega_2 \pm \sqrt{(\omega_1 - \omega_2)^2 + 4\alpha^2}\}. \quad (17)$$

Because B must be one of the two solutions, x_{\pm} , the following condition must be satisfied for Eq. (16);

$$\pm \sqrt{(\omega_1 - \omega_2)^2 + 4\alpha^2} = -\frac{(\omega_1 - \omega_2)(\gamma_{e1} - \gamma_{e2}) + 4p\alpha\sqrt{\gamma_{e1}\gamma_{e2}}}{\gamma_{e1} + \gamma_{e2}}. \quad (18)$$

By squaring both sides of Eq. (18), the following conditions are obtained for the existence of the BIC;

$$p\alpha(\gamma_{e1} - \gamma_{e2}) = \sqrt{\gamma_{e1}\gamma_{e2}}(\omega_1 - \omega_2). \quad (19)$$

Substituting Eq. (19) into Eq. (8) and then solving Eq. (8) with respect to ω , we obtain the following solutions .

$$\omega = \begin{cases} \frac{1}{2}(\omega_1 + \omega_2) + \frac{p\alpha}{2}\left(\sqrt{\frac{\gamma_{e1}}{\gamma_{e2}}} + \sqrt{\frac{\gamma_{e2}}{\gamma_{e1}}}\right) - i(\gamma_{e1} + \gamma_{e2}), \\ \frac{1}{2}(\omega_1 + \omega_2) - \frac{p\alpha}{2}\left(\sqrt{\frac{\gamma_{e1}}{\gamma_{e2}}} + \sqrt{\frac{\gamma_{e2}}{\gamma_{e1}}}\right). \end{cases} \quad (20)$$

The latter solution represents the BIC, which does not have an imaginary part. Therefore, the BIC appears in the lower frequency branch when

$$p\alpha > 0, \quad (21)$$

whereas the BIC appears in the higher frequency branch when

$$p\alpha < 0. \quad (22)$$

This result is consistent with the FW theory [32].

The regions where the BIC appears in the dispersion diagram can be discussed based on Eqs. (19), (21), and (22). Consider the dispersion of ω_1 and ω_2 having positive and negative slopes, respectively as shown in Fig. 5. Let us first consider the case of $p\alpha > 0$, for which, from Eq. (19), the signs of $\omega_1 - \omega_2$ and $\gamma_1 - \gamma_2$ should be the same. Hence, $\omega_1 > \omega_2$ must be satisfied for $\gamma_{e1} > \gamma_{e2}$, corresponding to division (1) or (4) in Fig. 5(a), while $\omega_1 < \omega_2$ for $\gamma_{e1} < \gamma_{e2}$, corresponding to division (2) or (3) in Fig. 5(b). On the other hand, considering Eq. (21), the BIC appears on the lower branch for $p\alpha > 0$. Therefore, the BIC appears in division (4) in Fig. 5(a) for $\gamma_{e1} > \gamma_{e2}$ and division (3) in Fig. 5(b) for $\gamma_1 < \gamma_2$, respectively. The case of $p\alpha < 0$ can be analyzed in a similar way. For $\gamma_{e1} > \gamma_{e2}$ and $\gamma_{e1} < \gamma_{e2}$, the BIC appears in division (2) in Fig. 5(a) and division (1) in Fig. 5(b), respectively. We further note that in both cases, the BIC appears on the mode with the lower radiative loss.

Next, let us check the correspondence between the above argument and the result in our structure shown in Fig. 4. In the case of P-wave excitation shown in Fig. 4(a), we can see that the TM_0 (ω_1) mode with positive slope is narrower than the TM_1 (ω_2) mode with negative slope, namely $\gamma_{e1} < \gamma_{e2}$ corresponding to Fig. 5(b), and the BIC is located on the branch in division (3), as confirmed by the fitting shown in Fig. 4(c). Hence, the above argument predicts $p\alpha > 0$. In the case of S-wave excitation, it is clear from Fig. 4(b) that the linewidth of the TE_0 (ω_1) mode is much narrower than the TE_1 (ω_2) mode, namely $\gamma_{e1} < \gamma_{e2}$ corresponding again to Fig. 5(b), and the BIC appears in division (1). Therefore, $p\alpha < 0$ is predicted. In the next subsection, we will confirm the above prediction, $p\alpha > 0$ and $p\alpha < 0$ for the P-wave and S-wave excitations, respectively, in our specific structure, by checking the signs of p and α from the SCMT calculation.

4.2. Evaluation of the signs of p and α using SCMT

As shown in the preceding section, the branch on which the BIC appears depends on the sign of $p\alpha$. Here, p denotes the phase difference (sign) between the coefficients that couple the waveguide modes with the external radiation; $p = 1$ and -1 means $\varphi_1 - \varphi_2 = 0$ and π , respectively. The phase difference between the two waveguide modes excited by the incident radiation is determined solely by these coupling coefficients, if the effects of near- and far-field couplings are negligible. Thus, the sign p can be evaluated easily from the phases of the excited waveguide modes. On the other hand, α represents the near field (direct) coupling between two resonant modes. As shown below, the $\text{sign}(\alpha)$ can also be found by inspecting the phases of the waveguide modes that construct the coupled resonant modes at the anti-crossing point.

We determine the phase of the waveguide modes from the actual SCMT simulation. Assume that the electric and magnetic fields inside the dielectric layer is expanded by

the propagating waveguide modes in the flat metal/dielectric/metal waveguide as [49]

$$\begin{aligned}\mathbf{E}(x, z) &= a_{1+}\mathbf{E}_{1+}(x, z) + a_{2+}\mathbf{E}_{2+}(x, z) + \cdots \\ &\quad + a_{1-}\mathbf{E}_{1-}(x, z) + a_{2-}\mathbf{E}_{2-}(x, z) + \cdots, \\ \mathbf{H}(x, z) &= a_{1+}\mathbf{H}_{1+}(x, z) + a_{2+}\mathbf{H}_{2+}(x, z) + \cdots \\ &\quad + a_{1-}\mathbf{H}_{1-}(x, z) + a_{2-}\mathbf{H}_{2-}(x, z) + \cdots.\end{aligned}\tag{23}$$

Here, $\mathbf{E}_{i\pm}$, $\mathbf{H}_{i\pm}$ represents the transverse components (in y - z plane in Fig. 1) of the electric and magnetic fields of the i -th waveguide mode, respectively, and the signs $+$ and $-$ denote the mode propagating in the $+x$ and $-x$ directions, respectively. $a_{i\pm}$ represents the complex amplitude of each waveguide mode. As seen in Fig. 2, only two modes are relevant near the BIC point. Hence, Eq. (23) can be simplified to

$$\begin{aligned}\mathbf{E}(x, z) &= a_{1s}\mathbf{E}_{1s}(x, z) + a_{2s'}\mathbf{E}_{2s'}(x, z), \\ \mathbf{H}(x, z) &= a_{1s}\mathbf{H}_{1s}(x, z) + a_{2s'}\mathbf{H}_{2s'}(x, z),\end{aligned}\tag{24}$$

where s and s' are either $+$ or $-$. In the case of Fig. 2(a) for the P-wave radiation, mode 1 and mode 2 correspond to the TM_0 mode propagating in $+x$ direction and the TM_1 mode propagating $-x$ direction, respectively. In the case of Fig. 2(b) for the S-wave radiation, they correspond to the TE_0 mode propagating in $+x$ direction and the TE_1 mode propagating in $+x$ direction, respectively. The direction of propagation was determined from the slope of the corresponding empty lattice mode. The amplitude a_{is} is obtained by

$$a_{is} = \int dz \left(\frac{\mathbf{E} \times \mathbf{H}_{is}^* + \mathbf{E}_{is}^* \times \mathbf{H}}{\mathbf{E}_{is} \times \mathbf{H}_{is}^* + \mathbf{E}_{is}^* \times \mathbf{H}_{is}} \right),\tag{25}$$

using the electric field \mathbf{E} and the magnetic field \mathbf{H} obtained by the actual SCMT calculation. The integration is performed over the dielectric region.

4.3. Evaluation of p

We evaluate the phase difference at the wavelength where the anti-crossing occurs, $k_x = 0.1905$ [π/Λ] and 0.1600 [π/Λ] for the P-wave and S-wave excitations, respectively. The calculated phase difference in SCMT is shown in Figs. 6(a) and 6(b) for the P-wave and S-wave cases, respectively. We denote the upper and lower branch of the coupled resonant wavelength as ω_+ and ω_- , respectively. Around ω_+ or ω_- , the phase difference between the waveguide modes varies rapidly due to the influence of the excitation of each resonator. However, in the region far from ω_+ and ω_- , the phase difference shows a convergence to 0 for the P-polarization and π for the S-polarization. In this region, the phase difference (sign) between the resonances should coincide with p , because the effect of the resonances on the phase difference is considered to be negligible (see Appendix).

For comparison, the phase differences were also calculated in TCMT. Figure 6(c) is the phase difference for $p = 1$ using the same parameters as for Fig. 4(c), and Fig. 6(d) is that for $p = -1$ with the parameters for Fig. 4(d). The overall behavior of the phase difference in the SCMT results (Figs. 6 (a) and (b)) corresponds very well to that

in the TCMT results (Fig. 6 (c) and (d)). Therefore, it can be concluded that $p = 1$ and $p = -1$ for the P- and S-polarizations, respectively.

4.4. Evaluation of α

The sign of α can be deduced from the phase of the eigenmode (quasi-bound mode). In our strong near-field coupling system, the eigenmode is mainly determined by α near the anti-crossing point. In TCMT, by equating the eigenfrequencies of the two resonant modes, $\omega_1 = \omega_2 = \omega_{12}$, and neglecting $\mathbf{\Gamma}_i$ and $\mathbf{\Gamma}_e$, we have the eigenfrequencies ω_+ and ω_- from

$$|\mathbf{\Omega} - \omega\mathbf{I}| = 0, \quad (26)$$

as

$$\omega_{\pm} = \omega_{12} \pm |\alpha|, \quad (27)$$

and the eigenvectors are derived from

$$\begin{pmatrix} \omega_{12} - \omega & \alpha \\ \alpha & \omega_{12} - \omega \end{pmatrix} \begin{pmatrix} a_1 \\ a_2 \end{pmatrix} = 0. \quad (28)$$

Hence, for $\alpha > 0$,

$$a_1 = a_2 \text{ for } \omega_+, \quad a_1 = -a_2 \text{ for } \omega_- \quad (29)$$

and when $\alpha < 0$ we have,

$$a_1 = -a_2 \text{ for } \omega_+, \quad a_1 = a_2 \text{ for } \omega_- \quad (30)$$

Therefore, the sign of α can also be evaluated from the phase difference $\arg(a_1) - \arg(a_2)$ at ω_+ or ω_- around the anti-crossing point. Here ω_1 and ω_2 correspond to either TM_0 (TE_0) or TM_1 (TE_1) for the P (S)-wave case. We evaluated a_1 and a_2 from the electric field in the same way as 4.2.1 using Eq. (25). The electric field of the coupled resonant modes can be obtained numerically by searching for the electromagnetic wave solution in the absence of the incident wave using SCMT. In the calculation, we eliminated the metal loss of the whole structure. Table 1(a) shows the results for the P-wave excitation at $k_x = 0.1905 [\pi/\Lambda]$ and Table 1(b) shows those for the S-wave case at $k_x = 0.1600 [\pi/\Lambda]$. In both cases, the phase difference is about 0 at ω_+ and π at ω_- , respectively. Therefore, it can be concluded that α is positive for both polarizations .

4.5. Sign of $p\alpha$

As shown above, $p = 1$ and $p = -1$ for the P- and S-polarizations, respectively and α is positive for both cases. Although $\text{sign}(p)$ can be changed by the redefinition of the phase of one of the waveguide modes, this change must be accompanied by the change of $\text{sign}(\alpha)$ with $\text{sign}(p\alpha)$ unchanged [48]. Hence, we can conclude that $\text{sign}(p\alpha)$ is positive in the P-polarization and negative in the S-polarization in our structure, demonstrating that the prediction by the TCMT stated in Section 4.1 is correct.

5. Conclusion

In conclusion, we discussed, for the first time, the branch on which the FW-BIC appears in the anti-crossing dispersion of a photonic system with a simple and practically important structure, namely dielectric waveguide with metal grating. We demonstrated that the branch is selected by the incident polarization. The mechanism was explained by TCMT in terms of the polarization-dependent phase relation between the relevant waveguide modes forming the BIC. The polarization dependence of the BIC formation in our simple structure implies the external controllability of BICs in various optical and photonic devices. However, a question still remains whether the plasmonic nature plays an important role in our structure, which is important not only from a viewpoint of optical physics, but also for various applications, because non-plasmonic structures may be better to obtain higher Q values. Although an answer has not been obtained, our discussion based on the TCMT applies regardless of the presence of the plasmonic effect, implying that the same or similar control of BICs is possible in various devices including all dielectric ones.

Acknowledgements

This work was supported by JSPS KAKENHI Grant Numbers JP18K04979 and JP18K04980.

Appendix

Consider a case that \mathbf{a} is time harmonic, $\mathbf{a} \propto e^{-i\omega t}$. Eq. (1) is written as

$$[i(\boldsymbol{\Omega} - \omega\mathbf{I}) + \boldsymbol{\Gamma}_i + \boldsymbol{\Gamma}_e]\mathbf{a} = \mathbf{D}^T s_+. \quad (\text{A.1})$$

Taking the inverse matrix from the left side of Eq. (A.1),

$$\mathbf{a} = [i(\boldsymbol{\Omega} - \omega\mathbf{I}) + \boldsymbol{\Gamma}_i + \boldsymbol{\Gamma}_e]^{-1}\mathbf{D}^T s_+. \quad (\text{A.2})$$

Substitute this into Eq. (2),

$$r(\omega) \equiv \frac{s_-}{s_+} = c_a + \mathbf{D}[i(\boldsymbol{\Omega} - \omega\mathbf{I}) + \boldsymbol{\Gamma}_i + \boldsymbol{\Gamma}_e]^{-1}\mathbf{D}^T. \quad (\text{A.3})$$

Under the condition of Eq. (3) and Eq. (4), inverse matrix is

$$[i(\boldsymbol{\Omega} - \omega\mathbf{I}) + \boldsymbol{\Gamma}_i + \boldsymbol{\Gamma}_e]^{-1} = \frac{\begin{pmatrix} i(\omega_1 - \omega) + \gamma_{i1} + \gamma_{e1} & i\alpha + p\sqrt{\gamma_{e1}\gamma_{e2}} \\ i\alpha + p\sqrt{\gamma_{e1}\gamma_{e2}} & i(\omega_2 - \omega) + \gamma_{i2} + \gamma_{e2} \end{pmatrix}}{\{(\omega_1 - \omega) - i(\gamma_{i1} + \gamma_{e1})\}\{(\omega_2 - \omega) - i(\gamma_{i2} + \gamma_{e2})\} + (i\alpha + p\sqrt{\gamma_{e1}\gamma_{e2}})^2}. \quad (\text{A.4})$$

After the matrix calculation on the RHS of Eq. (A.3), we finally get $r(\omega)$ as

$$r(\omega) = c_a \left[1 + 2 \frac{\gamma_{e1}\{i(\omega_2 - \omega) + \gamma_{i2}\} + \gamma_{e2}\{i(\omega_1 - \omega) + \gamma_{i1}\} - i2p\alpha\sqrt{\gamma_{e1}\gamma_{e2}}}{\{(\omega_1 - \omega) - i(\gamma_{i1} + \gamma_{e1})\}\{(\omega_2 - \omega) - i(\gamma_{i2} + \gamma_{e2})\} + (i\alpha + p\sqrt{\gamma_{e1}\gamma_{e2}})^2} \right]. \quad (\text{A.5})$$

On the other hand, the amplitudes of each mode can be obtained from Eq. (A.2) as

$$a_1 = \frac{\{i(\omega - \omega_2) - (\gamma_{i2} + \gamma_{e2})\}\sqrt{2\gamma_{e1}} + (p\sqrt{\gamma_{e1}\gamma_{e2}} + i\alpha)p\sqrt{2\gamma_{e2}}}{\{\omega - \omega_1 + i(\gamma_{i1} + \gamma_{e1})\}\{\omega - \omega_2 + i(\gamma_{i2} + \gamma_{e2})\} - (ip\sqrt{\gamma_{e1}\gamma_{e2}} - \alpha)^2} s_+, \quad (\text{A.6})$$

$$a_2 = \frac{\{i(\omega - \omega_1) - (\gamma_{i1} + \gamma_{e1})\}p\sqrt{2\gamma_{e2}} + (p\sqrt{\gamma_{e1}\gamma_{e2}} + i\alpha)\sqrt{2\gamma_{e1}}}{\{\omega - \omega_1 + i(\gamma_{i1} + \gamma_{e1})\}\{\omega - \omega_2 + i(\gamma_{i2} + \gamma_{e2})\} - (ip\sqrt{\gamma_{e1}\gamma_{e2}} - \alpha)^2} s_+. \quad (\text{A.7})$$

If $|\omega - \omega_1|$ and $|\omega - \omega_2|$ are much larger than the loss and the coupling coefficients, the amplitudes are approximated by

$$a_1 \simeq \frac{i\sqrt{2\gamma_{e1}}}{\omega - \omega_1} s_+, \quad (\text{A.8})$$

$$a_2 \simeq p \frac{i\sqrt{2\gamma_{e2}}}{\omega - \omega_2} s_+. \quad (\text{A.9})$$

Thus, the phase difference between a_1 and a_2 is determined by p in the region far from resonances where the signs of $\omega - \omega_1$ and $\omega - \omega_2$ are the same.

- [1] Hsu C W, Zhen B, Stone A D, Joannopoulos J D and Soljačić M 2016 Bound states in the continuum *Nat. Rev. Mat.* **1** 16048
- [2] Koshelev K, Favraud G, Bogdanov A, Kivshar Y and Fratallocchi A 2019 Nonradiating photonics with resonant dielectric nanostructures *Nanophotonics* **8** (5) 725-45
- [3] von Neumann J and Wigner E 1929 Uber merkwürdige diskrete Eigenwerte. Uber das Verhalten von Eigenwerten bei adiabatischen Prozessen *Zh. Phys.* **30** 467-70
- [4] Lyapina A A, Maksimov D N, Pilipchuk A S and Sadreev A F 2015 Bound states in the continuum in open acoustic resonators *J. Fluid. Mech.* **780** 370-387
- [5] Sadreev A F, Pilipchuk A S, and Lyapina A A 2017 Tuning of Fano resonances by rotation of continuum: Wave faucet *EPL* **117** 50011
- [6] Lyapina A A, Pilipchuk A S, and Sadreev A F 2018 Trapped modes in a non-axisymmetric cylindrical waveguide *J. Sound Vib.* **421** 48-60
- [7] Linton C M, and McIver P. 2007 Embedded trapped modes in water waves and acoustics *Wave motion* **45** (1-2) 16-29
- [8] Cobelli P J, Pagneux V, Maurel A and Petitjeans P 2011 Experimental study on water-wave trapped modes *J. Fluid Mech.* **666** 445-76
- [9] Wang Y, Song J, Dong L and Lu M 2016 Optical bound states in slotted high-contrast gratings *J. Opt. Soc. Am. B* **33** 122472
- [10] Bulgakov E N, Maksimov D N, Semina P N and Skorobogatov S A 2018 Propagating bound states in the continuum in dielectric gratings *JOSA B* **35** (6) 1218-22
- [11] Romano S, Zito G, Torino S, Calafiore G, Penzo E, Coppola G, Cabrini S, Rendina I and Mocella V 2018 Label-free sensing of ultralow-weight molecules with all-dielectric metasurfaces supporting bound states in the continuum *Photonics Research* **6** 726-33
- [12] Koshelev K, Lepeshov S, Liu M, Bogdanov A and Kivshar Y 2018 Asymmetric metasurfaces with high-Q resonances governed by bound states in the continuum *Phys. Rev. Lett.* **121** 193903
- [13] Cong L and Singh R 2019 Symmetry protected Dual Bound States in the Continuum in Metamaterials *Adv. Opt. Mat.* **7** 1900383.
- [14] Blanchard C, Hugonin J P and Sauvan C 2016 Fano resonances in photonic crystal slabs near optical bound states in the continuum *Phys. Rev. B* **94** 155303
- [15] Li L and Yin H 2016 Bound States in the Continuum in double layer structures *Sci. Rep.* **6** 26988
- [16] Hsu C W, Zhen B, Chua S, Johnson S G, Joannopoulos J D and Soljačić M 2013 Bloch surface eigenstates within the radiation continuum *Light: Science & Applications* **2** (7) e84
- [17] Yang Y, Peng C, Liang Y, Li Z and Noda S 2014 Analytical perspective for bound states in the continuum in photonic crystal slabs *Phys. Rev. Lett.* **113** 037401
- [18] Ni L, Wang Z, Peng C and Li Z 2016 Tunable optical bound states in the continuum beyond in-plane symmetry protection *Phys. Rev. B* **94** 245148
- [19] Silveirinha M G 2014 Trapping light in open plasmonic nanostructures *Phys. Rev. A* **89** 023813
- [20] Yoon J W, Song S H and Magnusson R. 2015 Critical field enhancement of asymptotic optical bound states in the continuum *Sci. Rep.* **5** 18301
- [21] Zhang W, Charous A, Nagai M, Mittleman D M and Mendis R. 2018 Extraordinary optical reflection resonances and bound states in the continuum from a periodic array of thin metal plates *Opt. Exp.* **26** (10) 13195-204
- [22] Fan K, Shadrivov I V and Padilla W J 2019 Dynamic bound states in the continuum *Optica* **6** (2) 169-73
- [23] Kodigala A, Lepetit T, Gu Q, Bahari B, Fainman Y and Kant B 2017 Lasing action from photonic bound states in continuum *Nature* **541** 11196
- [24] Ha S T, Fu Y H, Emani N K, Pan Z, Bakker R M, Paniagua-Domnguez R and Kuznetsov A I 2018 Directional lasing in resonant semiconductor nanoantenna arrays *Nature nanotech.* **13** (11) 1042
- [25] Zhang J, Kosugi Y, Otomo A, Nakano Y, and Tanemura T 2017 Active metasurface modulator with electro-optic polymer using bimodal plasmonic resonance *Opt. Exp.* **25** (24) 30304-311

- [26] Foley J M, Young S M and Phillips J D 2014 Symmetry-protected mode coupling near normal incidence for narrow-band transmission filtering in a dielectric grating *Phys. Rev. B* **89** 165111
- [27] Krasikov S D, Bogdanov A A and Iorsh I V 2018 Nonlinear bound states in the continuum of a one-dimensional photonic crystal slab *Phys. Rev. B* **97** 224309
- [28] Wang T and Zhang S 2018 Large enhancement of second harmonic generation from transition-metal dichalcogenide monolayer on grating near bound states in the continuum *Opt. Exp.* **26** (1) 322-337
- [29] Sadrieva Z F, Sinev I S, Koshelev K L, Samusev A, Iorsh I V, Takayama O, Malureanu R, Bogdanov A A and Lavrinenko A V 2017 Transition from optical bound states in the continuum to leaky resonances: role of substrate and roughness *ACS Photonics* **4** (4) 723-27
- [30] Wang H F, Gupta S K, Zhu X Y, Lu M H, Liu X P and Chen Y F 2018 Bound states in the continuum in a bilayer photonic crystal with TE-TM cross coupling *Phys. Rev. B* **98** 214101
- [31] Marinica D C, Borisov A G and Shabanov S V 2008 Bound States in the Continuum in Photonics *Phys. Rev. Lett.* **100** 183902
- [32] Friedrich H and Wintgen D 1985 Interfering resonances and bound states in the continuum *Phys. Rev. A* **32** 063231
- [33] Lepetit T and Kant B 2014 Controlling multipolar radiation with symmetries for electromagnetic bound states in the continuum *Phys. Rev. B* **90** 241103
- [34] Bogdanov A A, Koshelev K L, Kapitanova P V, Rybin M V, Gladyshev S A, Sadrieva Z F, Samusev K B, Kivshar Y S, and Limonova M F 2019 Bound states in the continuum and Fano resonances in the strong mode coupling regime *Adv. Photon.* **1** 016001
- [35] Rybin M V, Koshelev K L, Sadrieva Z F, Samusev K B, Bogdanov A A, Limonov M F and Kivshar Y S 2017 High-Q supercavity modes in subwavelength dielectric resonators *Phys. Rev. Lett.* **119** 243901
- [36] Bulgakov E N and Maksimov D N 2018 Avoided crossings and bound states in the continuum in low-contrast dielectric gratings *Phys. Rev. A* **98** 053840
- [37] Koshelev K L, Sychev S K, Sadrieva Z F, Bogdanov A A and Iorsh I V 2018 Strong coupling between excitons in transition metal dichalcogenides and optical bound states in the continuum *Phys. Rev. B* **98** 161113
- [38] Paddon P and Young J F 2000 Two-dimensional vector-coupled-mode theory for textured planar waveguides *Phys. Rev. B* **61** (3) 2090
- [39] Mermet-Lyaudoz R, Dubois F, Hoang N, Drouard E, Berguiga L, Seassal C, Letartre X, Viktorovitch P and Nguyen H S 2019 Realization of Bound state In the Continuum induced by vertical symmetry breaking in photonic lattice arXiv preprint arXiv:1905.03868
- [40] Azzam S I, Shalaev V M, Boltasseva A and Kildishev A V 2018 Formation of bound states in the continuum in hybrid plasmonic-photonic systems *Phys. Rev. Lett.* **121** 253901
- [41] Feshbach H 1958 Unified theory of nuclear reactions *Annals of Physics* **5** 4 357-90
- [42] Suh W, Wang Z and Fan S 2004 Temporal coupled-mode theory and the presence of non-orthogonal modes in lossless multimode cavities *IEEE Journal of Quantum Electronics* **40** (10) 1511-518
- [43] Fan S, Suh W and Joannopoulos J D 2003 Temporal coupled-mode theory for the Fano resonance in optical resonators *JOSA A* **20** (3) 569-72
- [44] Garcia-Vidal F J, Martin-Moreno L, Ebbesen T W and Kuipers L 2010 Light passing through subwavelength apertures *Rev. Mod. Phys.* **82** (1) 729
- [45] Nishida M, Hatakenaka N and Kadoya Y 2015 Multipole surface plasmons in metallic nanohole arrays *Phys. Rev. B* **91** 235406
- [46] Kikkawa R, Nishida M and Kadoya Y 2017 Substrate effects on the optical properties of metal gratings *JOSA B* **34** (12) 2578-85
- [47] Johnson P B and Christy R W 1972 Optical constants of the noble metals. *Phys. Rev. B* **6** 124370
- [48] Volya A and Zelevinsky V 2003 Non-Hermitian effective Hamiltonian and continuum shell model *Phys. Rev. C* **67** 054322
- [49] Snyder A W and Love J 1983 *Optical waveguide theory* Springer

Table 1. Phase difference between the two waveguide modes to determine the $\text{sign}(\alpha)$.(a) P-wave at $k_x = 0.1905 [\pi/\Lambda]$.

Branch	$\arg(a_{\text{TM}1-}) - \arg(a_{\text{TM}0+})$
ω_+	$3.45 \times 10^{-4}\pi$
ω_-	0.997π

(b) S-wave at $k_x = 0.1600 [\pi/\Lambda]$.

Branch	$\arg(a_{\text{TE}0+}) - \arg(a_{\text{TE}1+})$
ω_+	$-1.93 \times 10^{-2}\pi$
ω_-	0.989π

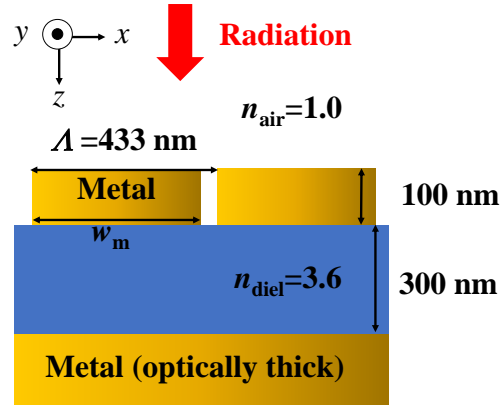


Figure 1. Cross sectional structure of the device considered in this work.

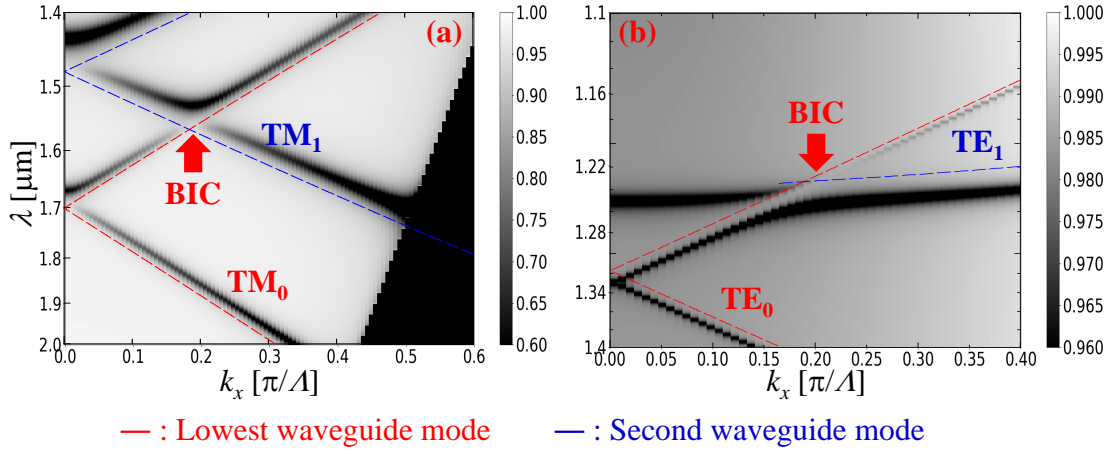


Figure 2. Reflectance as a function of the in-plane wave vector and the incident wavelength; (a) P-wave incidence, (b) S-wave incidence. The red arrows indicate the location of the BICs.

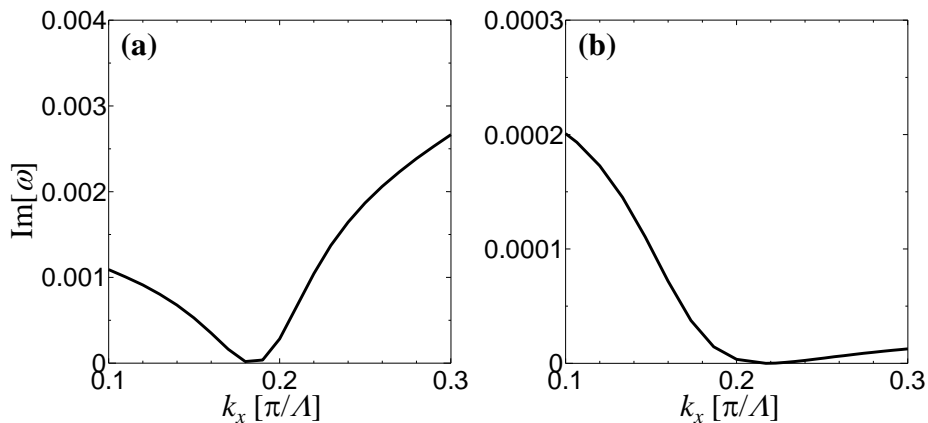


Figure 3. Imaginary part of the eigenfrequencies along the branch on which BIC appears; (a) P-wave (lower branch) and (b) S-wave (upper branch).

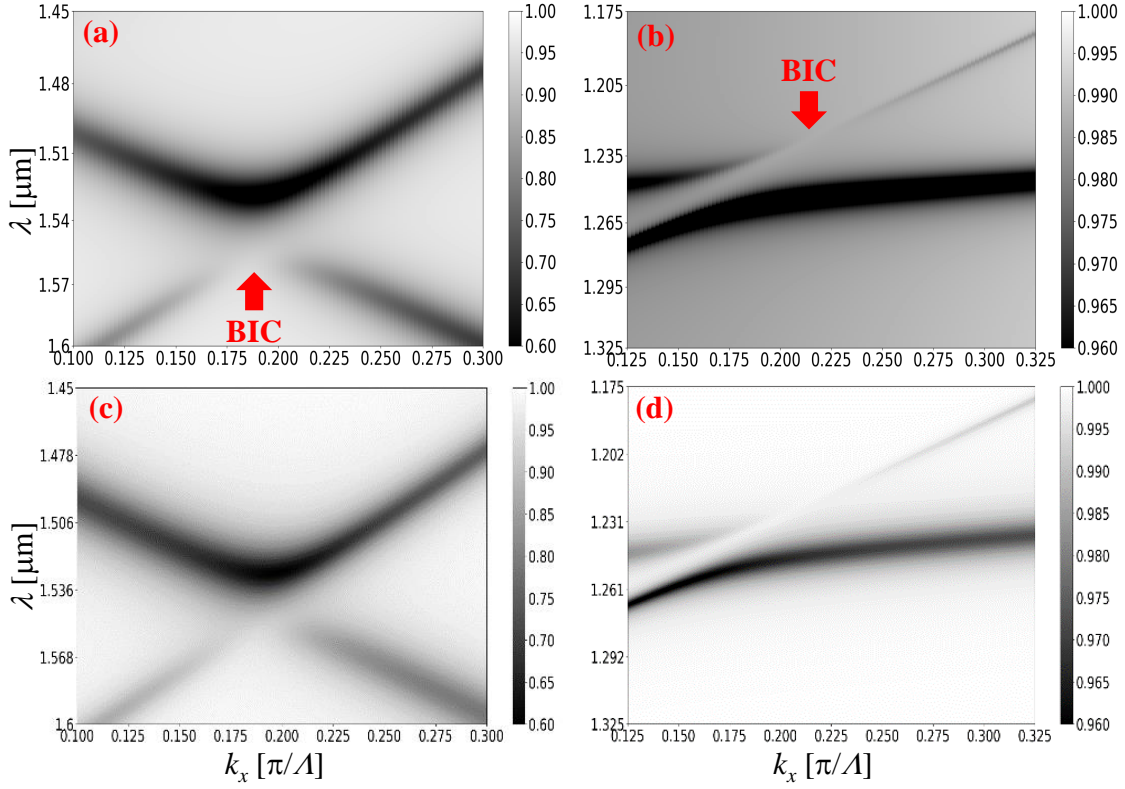


Figure 4. Reflectance as a function of the in-plane wave vector and the incident wavelength around the anti-crossing point. (a) P-wave and (b) S-wave redrawn from Figs. 2(a) and 2(b), respectively. The results of the TCMT calculation using Eq. (7) for (c) $p = 1$ and (d) $p = -1$ with the following parameters; (c) $\gamma_{i1}/c = 2.03 \times 10^{-2}$, $\gamma_{i2}/c = 3.15 \times 10^{-2}$, $\gamma_{e1}/c = 2.18 \times 10^{-3}$, $\gamma_{e2}/c = 4.42 \times 10^{-3}$, $\alpha/c = 3.52 \times 10^{-2}$, (d) $\gamma_{i1}/c = 6.24 \times 10^{-3}$, $\gamma_{i2}/c = 2.64 \times 10^{-2}$, $\gamma_{e1}/c = 5.77 \times 10^{-5}$, $\gamma_{e2}/c = 3.33 \times 10^{-4}$, $\alpha/c = 3.28 \times 10^{-2}$. Here c is the velocity of light in a vacuum.

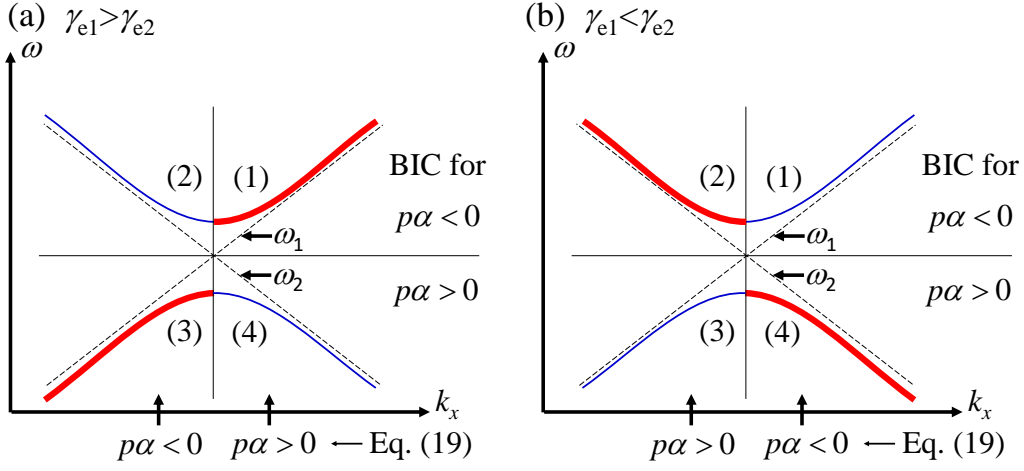


Figure 5. Illustration of the quadrant where BIC appears in the dispersion diagram near the anti-crossing point for (a) $\gamma_{e1} > \gamma_{e2}$ and (b) $\gamma_{e1} < \gamma_{e2}$. The red and blue lines depict the dispersions whose radiation loss is the larger (broad linewidth) and the smaller (narrow linewidth) of the two, respectively.

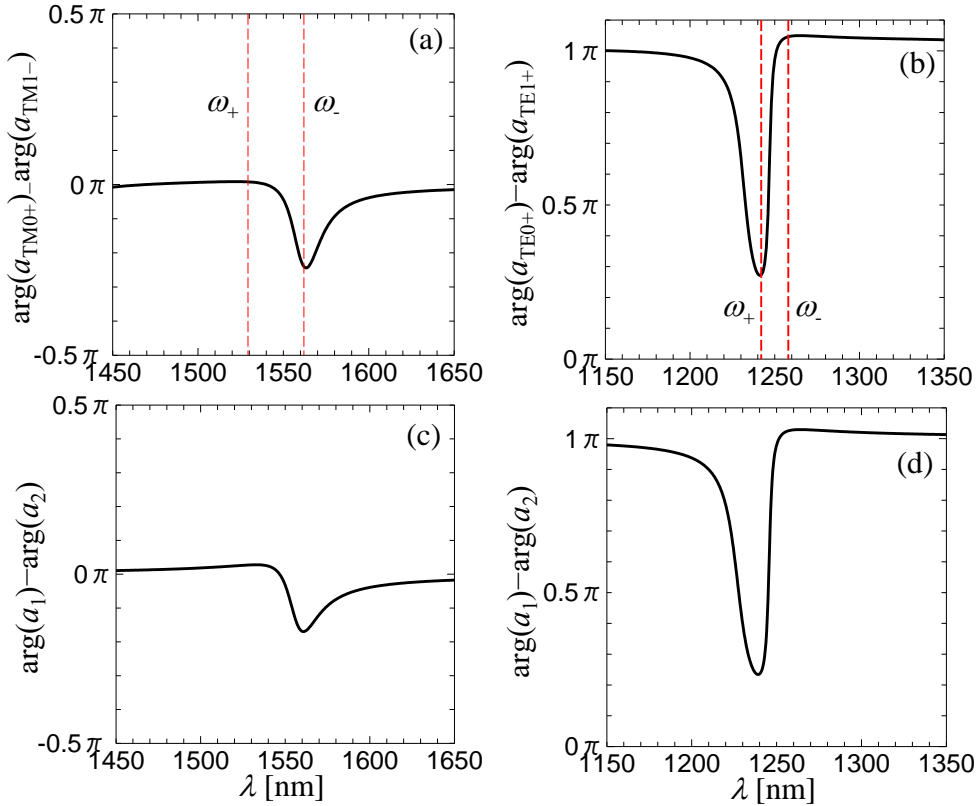


Figure 6. Phase difference of two modes excited by the external radiation; (a) P-wave at $k_x = 0.1905 [\pi/A]$ and (b) S-wave at $k_x = 0.1600 [\pi/A]$ by the SCMT calculations, (c) $p = 1$ and (d) $p = -1$ by the TCMT calculations. Red dashed lines in (a) and (b) indicate the wavelengths of the coupled resonant modes ω_+ and ω_- .